PNAS RESEARCH ARTICLE | BIOPHYSICS AND COMPUTATIONAL BIOLOGY

Molecular mechanism of fatty acid activation of FFAR1

Punita Kumari[a], Asuka Inoue[b], Karen Chapman[a], Peng Lian[c], and Daniel M. Rosenbaum[a,1]

Edited by Robert Lefkowitz, Howard Hughes Medical Institute, Durham, NC; received November 15, 2022; accepted April 3, 2023

FFAR1 is a G-protein-coupled receptor (GPCR) that responds to circulating free fatty acids to enhance glucose-stimulated insulin secretion and release of incretin hormones. Due to the glucose-lowering effect of FFAR1 activation, potent agonists for this receptor have been developed for the treatment of diabetes. Previous structural and biochemical studies of FFAR1 showed multiple sites of ligand binding to the inactive state but left the mechanism of fatty acid interaction and receptor activation unknown. We used cryo–electron microscopy to elucidate structures of activated FFAR1 bound to a G_q mimetic, which were induced either by the endogenous FFA ligand docosahexaenoic acid or γ-linolenic acid and the agonist drug TAK-875. Our data identify the orthosteric pocket for fatty acids and show how both endogenous hormones and synthetic agonists induce changes in helical packing along the outside of the receptor that propagate to exposure of the G-protein-coupling site. These structures show how FFAR1 functions without the highly conserved "DRY" and "NPXXY" motifs of class A GPCRs and also illustrate how the orthosteric site of a receptor can be bypassed by membrane-embedded drugs to confer full activation of G protein signaling.

fatty acid | GPCR | FFAR1 | insulin | cryoEM

Significance

FFAR1 is a physiologically important G-protein-coupled receptor (GPCR) and drug target that acts as a metabolic sensor and modulates insulin secretion. Despite numerous pharmacological and signaling investigations, the mechanism of fatty acid binding and activation of FFAR1 has remained unclear. In this study, we present structural and mutagenesis data that identify the fatty acid–binding pocket and show how these natural hormones activate the receptor. FFAR1 also presents an example of how different modes of membrane-embedded agonist binding can fully activate the same GPCR.

Free Fatty Acid Receptor 1 (FFAR1) Signaling and Pharmacology

FFAR1, also known as GPR40 helps to control energy homeostasis in mammals by sensing circulating medium and long-chain FFAs produced by lipolysis of dietary and endogenously synthesized triglycerides (1). When FFAs bind to FFAR1 on pancreatic β-cells and enteroendocrine cells, they activate signaling through G_q and β-arrestin (2). The consequences of this signal transduction are Ca^{2+} release into the cytosol, activation of protein kinase C, enhancement of insulin and incretin hormone release, glucose uptake, and lowering of plasma glucose levels (3, 4). FFAR1's primary physiological function is to sense the metabolic environment and regulate fuel utilization; however, the receptor is also expressed in other tissues such as the brain with roles in pain and inflammation (1). FFAR1 is the earliest deorphaned and most intensively studied member of the four GPCRs responding to FFAs, and it shares G_q signaling and FFA binding selectivity with FFAR4 (1, 2).

Due to the glucose-lowering effect of FFAR1 activation, a variety of synthetic agonists have been developed for the treatment of type two diabetes (5). One of these agonists, TAK-875, advanced to phase III clinical trials and demonstrated improvements in glycemic control and a low hypoglycemic risk profile; however, this drug was withdrawn from clinical development due to off-target liver toxicity (6). Two of the main natural ligands for FFAR1 are the omega-6 fatty acid γ-linolenic acid (γLA) and the omega-3 fatty acid docosahexaenoic acid (DHA). Drugs such as TAK-875 mimic these fatty acids functionally and chemically, acting as partial agonists and containing an extended hydrophobic group attached to a terminal carboxylic acid moiety (7). Whereas FFAs stimulate FFAR1 with potency in the micromolar range, TAK-875 and other FFAR1 agonist drugs have achieved EC_{50}s in the low nanomolar range (2, 7). Other synthetic FFAR1 agonists exemplified by AP8 and "compound 1" also contain a carboxylic acid; however, these drugs (also known as "AgoPAMs") act as full agonists and exhibit positive cooperativity with partial agonists such as TAK-875, and they bind to a different site on FFAR1 (8, 9). The complex pharmacology and overlapping chemical features of these different classes of agonists (2, 10) necessitate ligand-bound structures of activated FFAR1 to understand their distinct molecular mechanisms.

Structural Biology of FFAR1. The crystal structure of TAK-875 bound to FFAR1 in the inactive state (11) provided insights into the mechanism of agonist binding to the receptor. TAK-875 binds in an unusual mode for class A GPCRs, wedging between transmembrane (TM) helices 3 and 4 with its hydrophobic groups extending into the lipid bilayer and its carboxylic acid interacting with a cluster of arginine residues in

Author affiliations: [a]Department of Biophysics, The University of Texas Southwestern Medical Center, Dallas, TX 75390; [b]Department of Pharmaceutical Sciences, Tohoku University, Sendai 980-8578, Japan; and [c]BioHPC at the Lyda Hill Department of Bioinformatics, The University of Texas Southwestern Medical Center, Dallas, TX 75390

Author contributions: P.K., A.I., P.L., and D.M.R. designed research; P.K., A.I., K.C., and P.L. performed research; P.K., A.I., K.C., P.L., and D.M.R. analyzed data; and P.K. and D.M.R. wrote the paper.

The authors declare no competing interest.

This article is a PNAS Direct Submission.

[1]To whom correspondence may be addressed. Email: dan.rosenbaum@utsouthwestern.edu.

This article contains supporting information online at https://www.pnas.org/lookup/suppl/doi:10.1073/pnas.2219569120/-/DCSupplemental.

Published May 22, 2023.

the receptor core [R183$^{5.39}$ and R258$^{7.35}$, Ballesteros–Weinstein numbering (12) in superscript]. Subsequent structures of FFAR1 with both partial agonists and AgoPAMs AP8 (8) or compound 1 (9) identified an extrahelical ligand-binding site in the inner leaflet bounded by TM3, intracellular loop 2 (ICL2), TM4, and TM5, which is allosterically linked to the TAK-875 binding site. Because these structures were obtained using crystals of the inactive-state conformation, the mechanism of receptor activation has not been clarified. In addition, previous structural studies failed to provide direct insights into the binding of endogenous fatty acids to FFAR1.

In this study, we used cryo-EM to elucidate structures of activated FFAR1 in complex with a G_q-mimetic heterotrimer. These complexes were induced by different agonists including the natural ligand DHA and a combination of γLA and TAK-875. We also carried out mutagenesis and cell-based activation assays to probe the importance of different sites for activation by these agonists. Our structural and functional data show that fatty acids bind similarly to TAK-875 at the traditional class A GPCR orthosteric site. The binding of the agonists between TMs 3 and 4 leads to changes in helical packing that propagate through TMs 4 and 5, ultimately promoting a smaller outward movement of TM6 at a more cytosolic position compared to other class A GPCRs.

Results

Structure Determination of Activated FFAR1 Coupled to a G_q Mimetic. We solved structures of activated human FFAR1 bound to the mini-$G_{as/q/iN}$/$G_{\beta1}$/$G_{\gamma2}$ heterotrimer [referred to as mG_{sqiN} (13)], mimicking the receptor-G_q signaling complex leading to Ca^{2+}

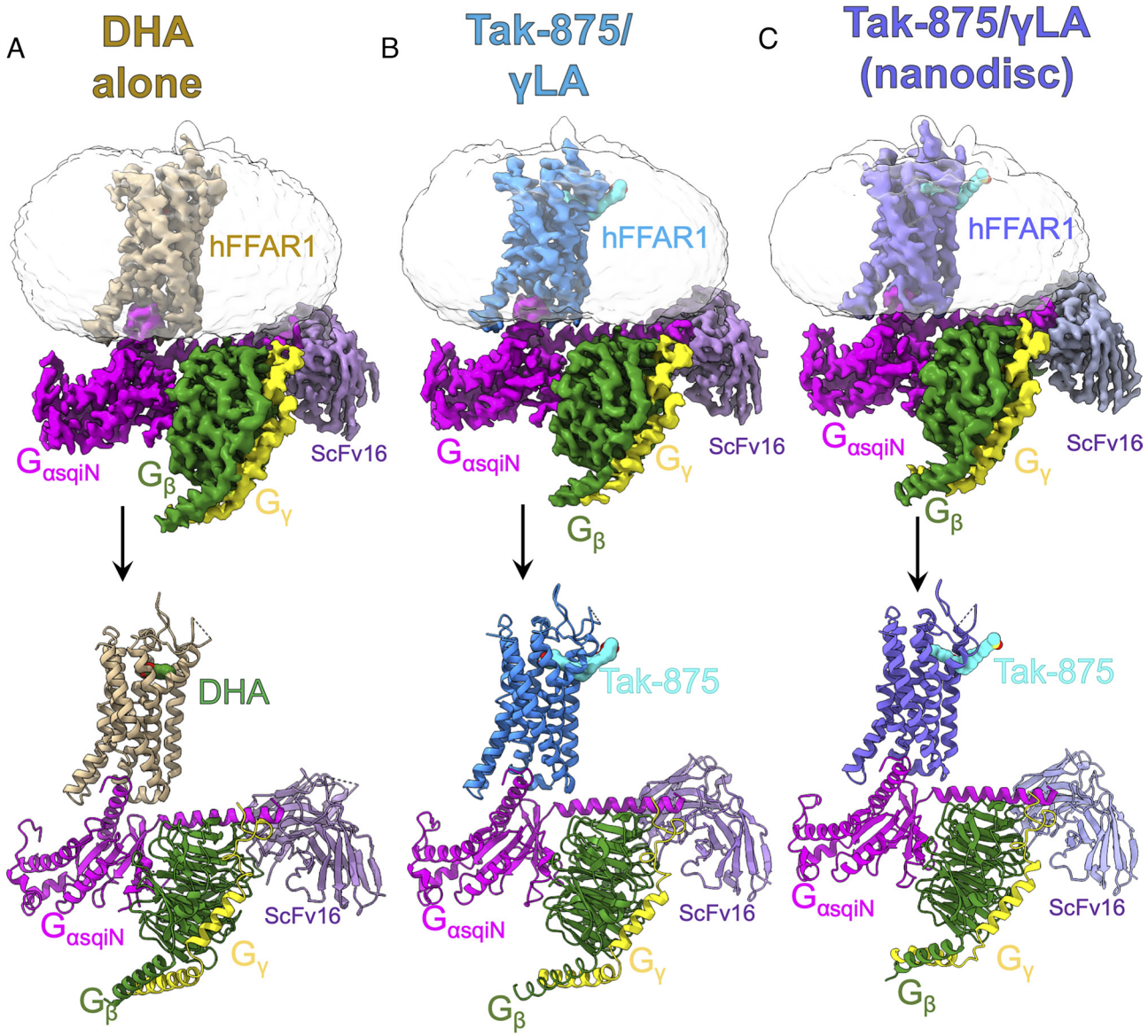

Fig. 1. Overall structures of activated FFAR1-G protein complexes. (*A, Top*) cryo-EM reconstruction of FFAR1-mG_{sqiN} bound to DHA. Receptor density is gold, mG_{sqiN} is magenta, $G_{\beta1}$ is green, $G_{\gamma2}$ is yellow, and scFv16 is purple. Cryo-EM density from Relion was displayed in Chimera as colored surfaces (contoured at 4.9 sigma), where different colored zones correspond to the different polypeptides. (*A*, *Bottom*) the corresponding model is shown as a cartoon, with DHA agonist in green spheres. (*B, Top*) cryo-EM reconstruction of FFAR1-mG_{sqiN} with TAK-875 and γLA. Receptor density is blue, mG_{sqiN} is magenta, $G_{\beta1}$ is green, $G_{\gamma2}$ is yellow, and scFv16 is purple. Cryo-EM density from Relion was displayed in Chimera as colored surfaces (contoured at 5.9 sigma), where different colored zones correspond to the different polypeptides. (*B*, *Bottom*) the corresponding model is shown as a cartoon, with TAK-875 agonist in cyan spheres. (*C*, *Top*) cryo-EM reconstruction of FFAR1-mG_{sqiN} with TAK-875 and γLA in lipid nanodisc. Receptor density is purple, mG_{sqiN} is magenta, $G_{\beta1}$ is green, $G_{\gamma2}$ is yellow, and scFv16 is purple. Cryo-EM density from Relion was displayed in Chimera as colored surfaces (contoured at 6.1 sigma), where different colored zones correspond to the different polypeptides. (*C*, *Bottom*) the corresponding model is shown as a cartoon, with TAK-875 agonist in cyan spheres.

release. The complex of FFAR1-mG_{sqiN} with DHA was purified in glyco-diosgenin (GDN) micelles from *Sf9* insect cells, and its cryo-EM structure was solved at 2.8 Å resolution (*SI Appendix*, Fig. S1). To investigate the cooperative activation by both TAK-875 and γLA reported in previous studies (14), we obtained structures for FFAR1-mG_{sqiN} in the presence of saturating concentrations of both ligands: one in GDN at 3.0 Å resolution (*SI Appendix*, Fig. S2) and one in phospholipid/cholesterol/MSP1D1 (15) nanodiscs at 3.4 Å resolution (*SI Appendix*, Fig. S3). All three structures used scFv16 (16) binding to aid in alignment of particles for cryo-EM reconstruction. The cryo-EM maps and atomic models for the three FFAR1-mG_{sqiN} complexes are shown in Fig. 1 *A*–*C*. Overall, there is very strong agreement between the atomic models, with pairwise rmsd of 0.6 to 0.8 Å overall and 0.5 to 0.7 Å for the receptor alone. Local resolution is lower for the extracellular half of the receptor in the FFAR1/TAK-875/γLA-mG_{sqiN} nanodisc map; however, side-chain density in the TM helices is still strong in this complex (*SI Appendix*, Fig. S4).

Fatty Acid Binding to Activated FFAR1. Previous molecular modeling (9, 17), cell-based assays (14), and inactive-state structures have provided conflicting evidence regarding the fatty acid–binding site on FFAR1. Early reports identified $R183^{5.39}$ and $R258^{7.35}$ as basic residues buried in the core of the receptor

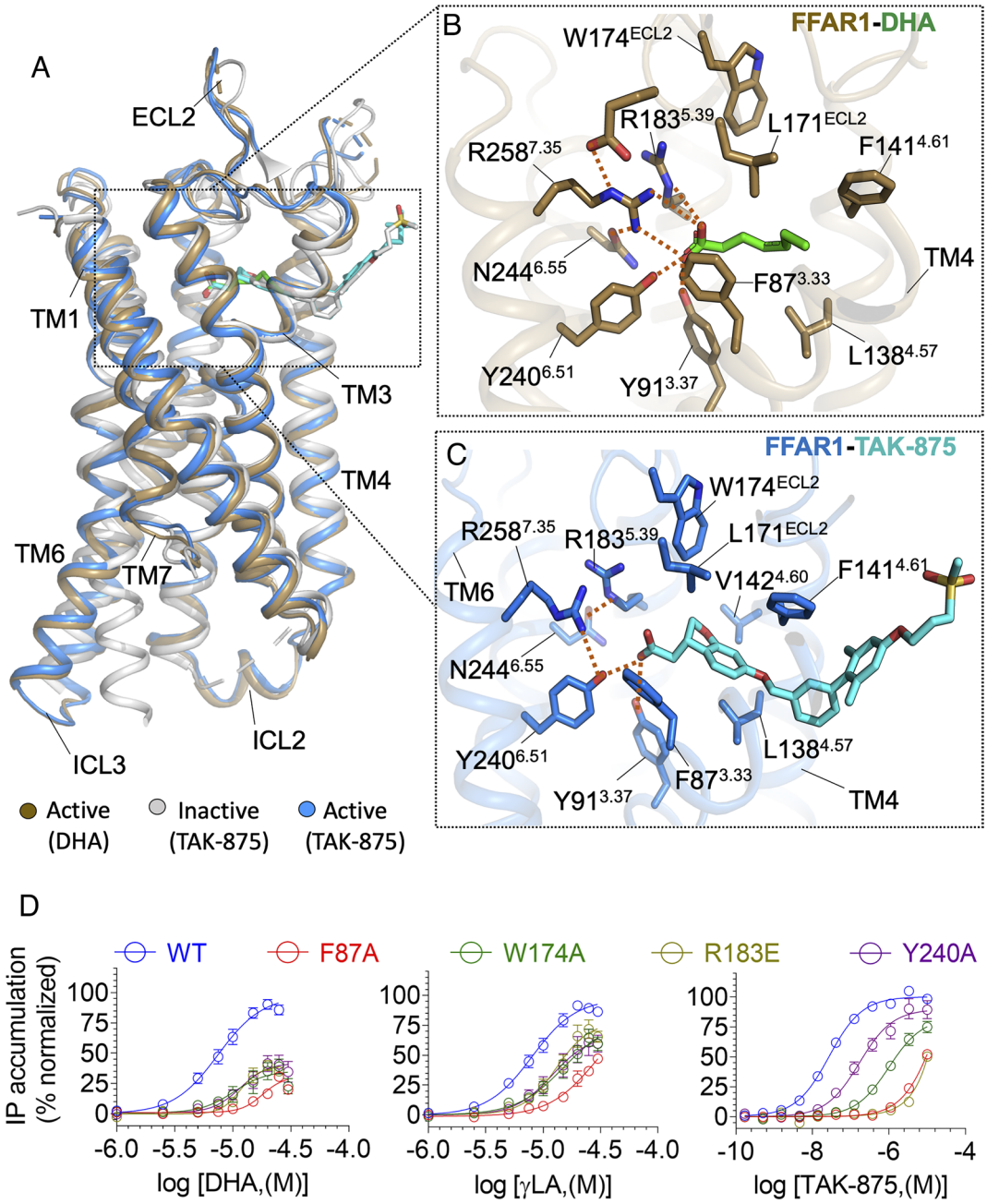

Fig. 2. Orthosteric ligand binding to activated FFAR1. (*A*) Superposition of activated FFAR1 bound to DHA (gold cartoon, green sticks), activated FFAR1 bound to TAK-875 (blue cartoon, cyan sticks), and inactive FFAR1 bound to TAK-875 (gray cartoon, gray sticks, PDB: 4PHU). (*B*) Contact residues (gold sticks) within 4 Å of DHA (green sticks) in activated FFAR1. Polar contacts within 4 Å are shown as dashed orange lines. (*C*) Contact residues (blue sticks) within 4 Å of TAK-875 (cyan sticks) in activated FFAR1. Polar contacts within 4 Å are shown as dashed orange lines. (*D*) Stimulation of G_q by FFAR1 wild type (WT) and mutants in response to DHA (*Left*), γLA (*Middle*), and TAK-875 (*Right*). Each data point in the IP accumulation assay represents the average from three or more independent experiments, each performed in duplicate. Error bars denote ± SEM. Data were normalized to the WT E_{max} and fitted to the four-parameter model "log(agonist) vs. response" in GraphPad Prism 9. Statistical parameters are shown in *SI Appendix*, Table S2A.

that are required for interaction with the carboxylate moiety on different FFAR1 agonists and also hypothesized that glutamate residues E145$^{4.64}$ and E172^{ECL2} on extracellular loop 2 (ECL2) could form "ionic locks" with these arginines that are broken during the activation process (17, 18). Later pharmacological studies using different FFAR1 ligands proposed as many as three distinct binding sites for acid-bearing agonists, with one group of agonists showing positive binding cooperativity with DHA and one showing negative cooperativity (19). Another study provided evidence that TAK-875 displays positive functional cooperativity with γLA (14), implying that fatty acids can bind at an alternative position to the TAK-875 site revealed in inactive-state structures. In addition, two previous crystal structures showed how AgoPAMs bind to the extrahelical site near ICL2 (8, 9), which could represent a possible site of FFA interaction.

Determining the structure of FFAR1 with a fatty acid ligand is inherently challenging due to the low potency of the endogenous agonists compared to synthetic drugs such as TAK-875, as well as the limited solubility of fatty acids in detergents used for receptor purification. We were able to overcome this barrier by including a high concentration of DHA in GDN micelles in our purification (*SI Appendix*, Fig. S5*A*), allowing the isolation of a G protein complex and a resulting 2.8 Å cryo-EM reconstruction. The map of activated FFAR1-mG$_{sqiN}$ with DHA contains density at a similar overall site in the receptor core as previously found for TAK-875 (which we denote as the "orthosteric site") (*SI Appendix*, Fig. S6*A*); however, we did not model 15 carbons of the aliphatic tail outside the receptor due to weaker density (Fig. 2*A*). The positions of the side chains of R183$^{5.39}$ and R258$^{7.35}$ are stabilized by a network of interactions with polar residues including E172^{ECL2} and N244$^{6.55}$, but not including the other putative "ionic lock" residue E145$^{4.64}$ (Fig. 2*B*). In our model, the fatty acid makes multiple buried hydrophobic contacts with residues including F87$^{3.33}$ and W174^{ECL2} (Fig. 2*B*).

To further validate whether DHA activates the receptor by binding to the core site within FFAR1, we carried out cell-based inositol phosphate (IP) accumulation assays for G$_q$ signaling. Mutations to the core polar network (R183$^{5.39}$E and Y240$^{6.51}$F) led to a reduction

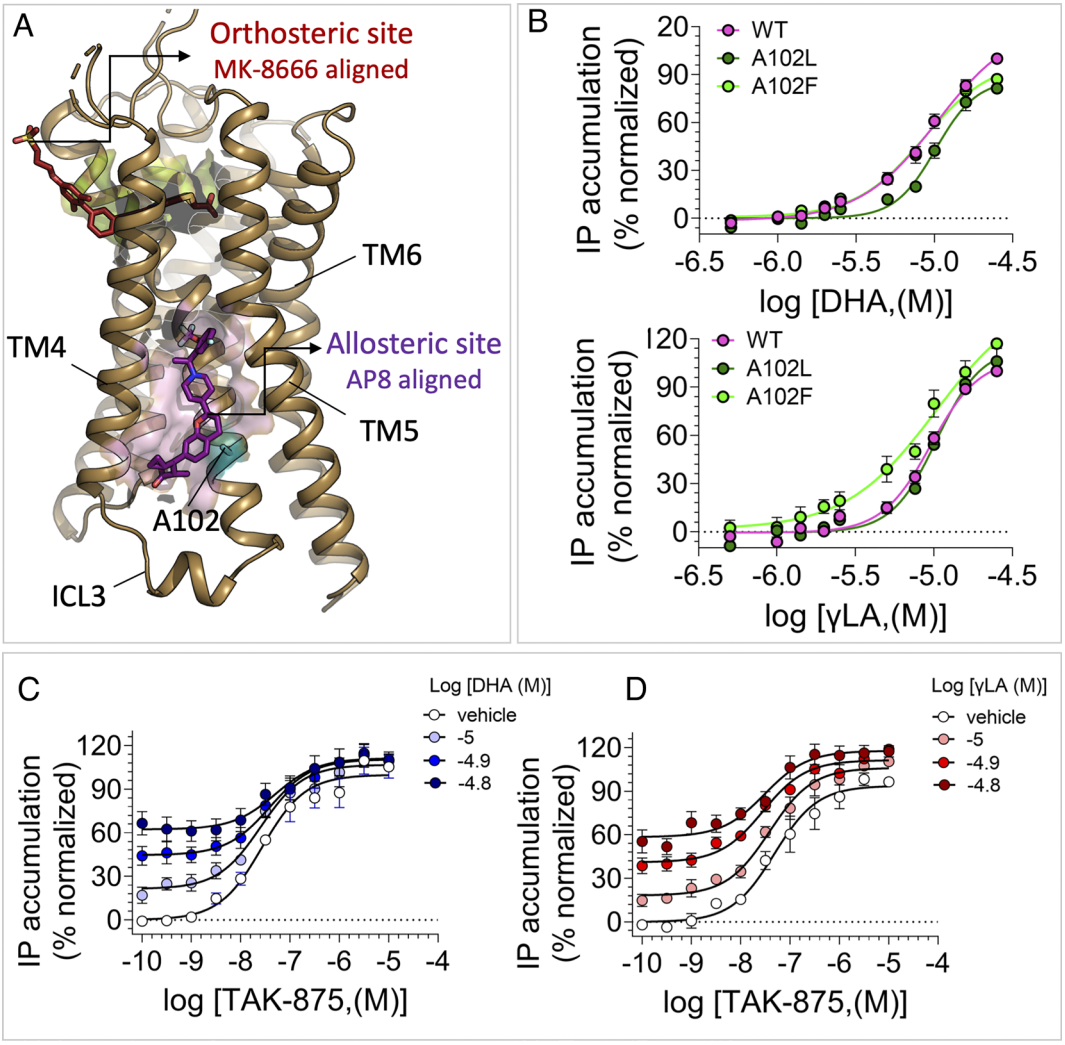

Fig. 3. Functional characterization of the allosteric site in activated FFAR1. (*A*) Position of orthosteric and allosteric sites mapped onto the structure of activated FFAR1 (gold cartoon, DHA complex). The predicted positions of orthosteric agonist MK-8666 (red sticks) and AgoPAM ligand AP8 (purple sticks) were determined by the superposition of the inactive FFAR1 structure (PDB 5TZY) with our activated DHA-bound FFAR1. (*B*) Stimulation of G$_q$ by FFAR1 wild type (WT) and A102$^{3.48}$ mutants in response to DHA (*Top*) or γLA (*Bottom*). Each data point in the IP accumulation assay represents the average from three or more independent experiments, each performed in duplicate. Error bars denote ± SEM. Data were normalized to the WT E$_{max}$ and fitted to the four-parameter model "log(agonist) vs. response" in GraphPad Prism 9. Statistical parameters are shown in *SI Appendix*, Table S2*C*. (*C-D*) Stimulation of G$_q$ by FFAR1 in response to TAK-875 in the presence of increasing concentrations of DHA (*C*) or γLA (*D*). Each data point in the IP accumulation assay represents the average from three or more independent experiments, each performed in duplicate. Error bars denote ± SEM. Data were normalized to the WT (E$_{max}$ defined as 100%) and fitted to the four-parameter model "log(agonist) vs. response" in GraphPad Prism 9. Statistical parameters are shown in *SI Appendix*, Table S2*B*.

in potency and maximal efficacy for DHA and γLA, as well as the drug TAK-875 (Fig. 2*D*, see also *SI Appendix*, Table S2*A*). We did not measure activity for mutations to $R258^{7.35}$ due to compromised receptor expression on Cos-7 cell membranes (*SI Appendix*, Fig. S7); however, previous mutation of $R258^{7.35}$ to alanine also showed a clear reduction in fatty acid potency (17). Likewise, the mutations $F87^{3.33}$A and $W174^{ECL2}$A in the core orthosteric binding site diminished G_q signaling by DHA, γLA, and TAK-875 (Fig. 2*D*), presumably by disrupting hydrophobic interaction with the agonists. In addition to mutations at the orthosteric site, we also tested the mutations $A102^{3.48}$F and $A102^{3.48}$L in the center of the extrahelical AgoPAM-binding site in the inner leaflet (Fig. 3*A*). These bulky substitutions would be expected to disrupt the specific interaction of an agonist such as DHA at this lipid-facing surface. Instead, our functional assays showed that the $A102^{3.48}$ mutations have little effect on either the potency or maximal efficacy of DHA or γLA (Fig. 3*B*). In parallel, we also carried out an assay in which G_q activation by a GPCR stimulates ectodomain shedding of a membrane-bound proform of alkaline phosphatase–tagged TGFα (20). These data agreed with the IP accumulation assay, indicating that $A102^{3.48}$F and $A102^{3.48}$L have little effect on fatty acid stimulation of FFAR1 (*SI Appendix*, Fig. S8*A*). Together with our cryo-EM data, these results indicate that the endogenous FFA agonists DHA and γLA, like the synthetic agonist TAK-875, bind at the core orthosteric site to activate FFAR1 and do not require binding at the extrahelical AgoPAM site. The unusual positioning of basic arginine side chains in the core of the receptor is adapted for electrostatic interaction with the carboxylic acid groups of endogenous FFA ligands, and this type of interaction has also been observed in soluble fatty acid–binding proteins (21).

TAK-875 Binding to Activated FFAR1. Despite our data regarding the orthosteric site of FFA binding and activation, it is still possible that FFAs could bind at additional sites to exert allosteric control over FFAR1 activation, supported by the previous findings of multiple binding sites for carboxylic acid–containing agonists (19) and putative cooperativity between γLA and TAK-875 (14). To search for additional fatty acid binding sites on FFAR1, we determined structures of the FFAR1-mG_{sqiN} complex in the presence of γLA and TAK-875, both above their saturating concentrations as determined by functional assays (Fig. 2*D*). In the structure elucidated in GDN micelles at 3.0 Å resolution, we again observe cryo-EM density at the orthosteric pocket that overlaps with that of DHA (Fig. 2*C*, see also *SI Appendix*, Fig. S6*C*). However, we did not obtain clear density at the previously identified AgoPAM site or other extrahelical surfaces. We placed TAK-875 at the orthosteric pocket in our resulting atomic model (Fig. 2 *A* and *C*), both because its affinity is far higher than that of γLA and because the density is in closer agreement with the features of TAK-875. The binding mode for TAK-875 in activated FFAR1 is similar to the previously reported structure of the drug bound to the inactive conformation (11) (Fig. 2*A*), with the caveat that cryo-EM density is weak for the sulfone-containing tail (*SI Appendix*, Fig. S6*C*). TAK-875 makes similar contacts with buried polar residues whose mutation leads to negative effects on potency (Fig. 2*C*). This model is further supported by the results of the $F87^{3.33}$ and $W174^{ECL2}$ mutations, which remove hydrophobic packing interactions at this pocket and reduce signaling stimulated by TAK-875 as well as fatty acids (Fig. 2*D*).

In addition to the GDN-based complex, we also determined the structure of FFAR1-mG_{sqiN} with γLA and TAK-875 reconstituted into phospholipid/cholesterol bilayer nanodiscs at 3.4 Å resolution (Fig. 1*C*). Overall, this structure is very similar to the complex in GDN (rmsd of 0.8 Å). In the bilayer, as in the GDN-based complex, there is no strong density for an additional ligand bound to an extrahelical surface such as the AgoPAM site. A caveat to these structural findings is that the binding of fatty acids at such extrahelical lipid-facing surfaces may be too dynamic to allow the identification of distinct cryo-EM density for the ligand. Although our structures failed to provide convincing evidence of simultaneous binding to FFAR1 of both γLA and TAK-875, we attempted to validate whether fatty acids display positive functional cooperativity in signaling. In both IP accumulation (Fig. 3 *C* and *D*) and TGFa shedding assays (*SI Appendix*, Fig. S8*B*), there is minimal effect on the EC_{50} of TAK-875 with increasing concentrations of γLA or DHA (see also *SI Appendix*, Table S2 *B* and *D*), implying that fatty acids do not bind at a different site to potentiate TAK-875 agonism.

To gain further insights into the mechanism of fatty acid entry into the orthosteric pocket of FFAR1, we carried out an all-atom molecular dynamics (MD) simulation of unliganded ("Apo") FFAR1 in a phospholipid/cholesterol bilayer, starting with the receptor conformation in the FFAR1/DHA-mG_{sqiN} complex (Fig. 4*A*). While the overall conformation of the receptor was stable over the course of the >200 nanosecond simulation, there was a significant local change in the positioning of the extracellular half of TM3 (Fig. 4*B*). Compared to other class A GPCRs, this region of TM3 in FFAR1 is bent outward toward the membrane to accommodate ligand binding between TMs 3 and 4. Without a ligand present in the simulation, TM3 quickly (over ~75 nanoseconds) moves to a more inward position that no longer allows ligand entry. In contrast, when bound DHA was included in the simulation, no inward movement of TM3 was seen (Fig. 4*A*). Intriguingly, the conformational change observed in our Apo simulation is reminiscent of the inward position of this same section of TM3 in the compound 1–bound FFAR1 structure without an orthosteric ligand (9). These MD results imply that fluctuations in the extracellular half of TM3 allow FFAR1 to continually sample the membrane for endogenous fatty acid agonists, and the active conformation becomes trapped with TM3 bent outward once a carboxylic acid–bearing agonist engages favorably in the core.

Activation Mechanism of FFAR1. The ultimate product of FFA or TAK-875 binding to the orthosteric site on FFAR1 is to stabilize a conformation of the receptor with outward movement of the

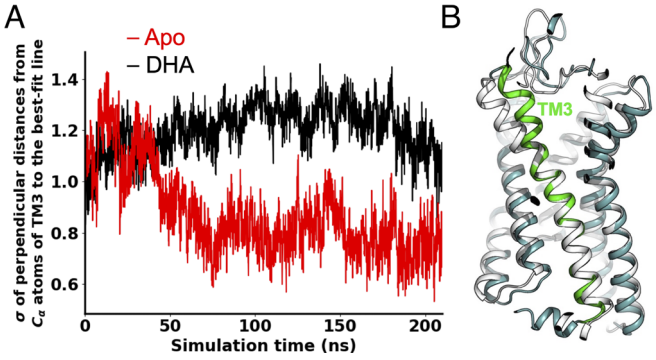

Fig. 4. Molecular dynamics (MD) simulation of activated FFAR1. (*A*) Plot of SD (σ) of perpendicular distances from all the C_α atoms of TM3 to the best-fit line of the C_α atoms, over time of the simulation. The red trace (Apo) corresponds to the simulation of the activated FFAR1 structure in the absence of the DHA ligand. The fast decline of the σ value starting with the activated structure (DHA complex) indicates that the extracellular half of TM3 becomes straighter during the first 75 nanoseconds of the MD simulation. The black trace (DHA) corresponds to the simulation of the activated FFAR1 structure starting with the DHA ligand intact. (*B*) Superposition of FFAR1 before (white cartoon) and after (cyan cartoon) the Apo MD simulation. TM3 at the end of the simulation is colored green to highlight the change in conformation of its extracellular half to become straighter in the absence of a ligand.

cytoplasmic end of TM6 that enables the G_q carboxy-terminal α5 helix to bind. In our structures of FFAR1 bound to mG_{sqiN}, as in other activated GPCR-G_q complexes, hydrophobic contacts are established between the cytoplasmic TM5-TM6 region of FFAR1 and the α5 helix of G_q with its C-terminal hook (22–25). Specifically, residues C205$^{5.61}$, L209$^{5.65}$, L214^{ICL3}, A222$^{6.33}$, and V225$^{6.36}$ from the receptor pack against L228$^{H5.16}$, L232$^{H5.20}$, L237$^{H5.25}$, and V238$^{H5.26}$ on the G protein (Fig. 5*A*, see also *SI Appendix*, Fig. S6*B*). Opposite to this largely hydrophobic interface, multiple specific polar contacts occur between ICL2 and the other face of the α5 helix: Y114^{ICL2} makes a hydrogen bond to Y235$^{H5.23}$ of G_q, Q115^{ICL2} makes a hydrogen bond to N231$^{H5.19}$, and R118^{ICL2} interacts electrostatically with E234$^{H5.22}$ (Fig. 5*A*). Polar contacts between the receptor ICL2 and the α5 helix may help to confer G_q selectivity, as similar interactions have been observed in other GPCR-G_q complexes (24, 25), and Y235$^{H5.23}$ is not present on other G proteins such as G_i. Unlike most other GPCRs, the highly conserved "NPXXY motif" is changed to NPLVT (residues 272-276) in FFAR1 (Fig. 5*B*). A tyrosine residue at the fifth position in this motif normally occupies a central position in the core of an activated GPCR above the G protein α5 helix (22, 26). Without this anchor, the cytoplasmic end of TM7 in FFAR1 is disordered and does not form part of the G_q-binding interface; however, Y278$^{7.55}$ in the extended loop at the end of TM7 forms a hydrogen bond with the backbone amide of E234$^{H5.22}$ of G_q. The lack of an ordered cytoplasmic end of TM7 (and Helix 8) allows the G_q α5 helix to bind where TM7 would normally sterically occlude it. Outward movement of TM6 to accommodate this interaction is smaller than in the β_2 adrenergic receptor(β_2AR)-G_s complex (27) or the M1 muscarinic receptor (M1R)-G_{11} complex (22) (Fig. 5*F*) and is facilitated by a

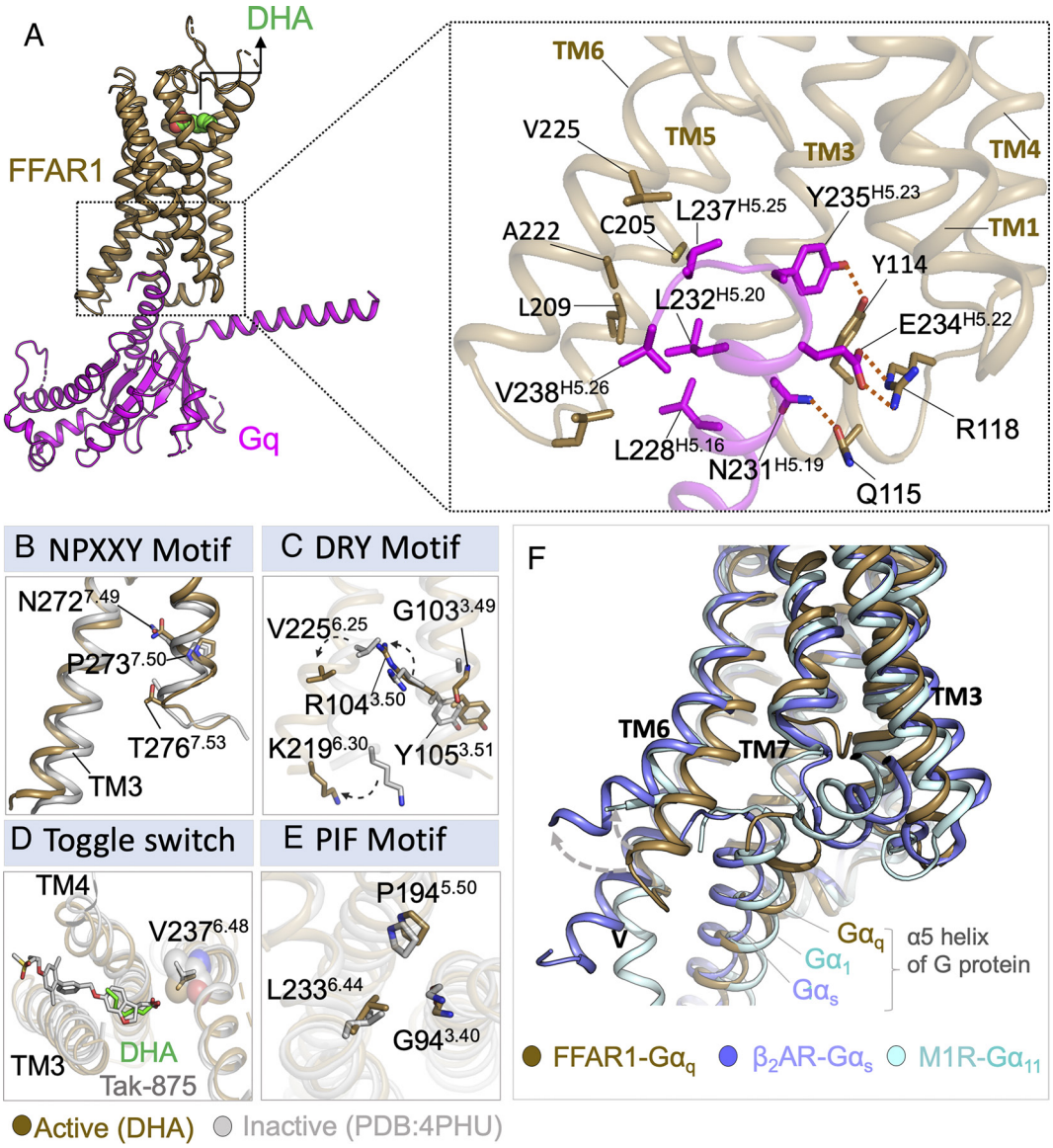

Fig. 5. Activation of FFAR1 and interface with G protein. (*A*) FFAR1–mG_{sqiN} complex bound to DHA. FFAR1 is a gold cartoon, G_α is magenta, and DHA is in green spheres. The *Inset* shows an enlarged view of the interface between FFAR1 and α5-helix of $G_{\alpha q}$, with FFAR1 residues as gold sticks and G_q residues as magenta sticks. Polar contacts <4 Å are highlighted as dashed orange lines. (*B*) Overlay of NPXXY motif between activated FFAR1 (DHA complex, residues shown as gold sticks) and inactive FFAR1 (PDB: 4PHU, residues shown as gray sticks). (*C*) Overlay of DRY motif between activated FFAR1 (DHA complex, residues shown as gold sticks) and inactive FFAR1 (PDB: 4PHU, residues shown as gray sticks). (*D*) Overlay of a toggle switch between activated FFAR1 (DHA complex, residues shown as gold sticks) and inactive FFAR1 (PDB: 4PHU, residues shown as gray sticks). (*E*) Overlay of PIF motif between activated FFAR1 (DHA complex, residues shown as gold sticks) and inactive FFAR1 (PDB: 4PHU, residues shown as gray sticks). (*F*) Superposition of receptors with G protein a5 helix in FFAR1-G_q (gold cartoon), β_2AR-G_s (slate blue cartoon, PDB:3SN6), and M1R-G_{11} (cyan cartoon, PDB: 6OIJ).

bend at the diglycine sequence G227$^{6.38}$-G228$^{6.39}$. As a measure of the difference in outward movement, the R104$^{3.50}$-A222$^{6.33}$ Cα-Cα distance in activated FFAR1-mG$_{sqiN}$ is 10.6 Å versus 14.6 Å for β_2AR-G$_s$ or 12.9 Å for M1R-G$_{11}$.

The highly conserved "E/DRY motif" in class A GPCRs normally participates in intrahelical (28) and interhelical (with an acidic residue 6.30 on TM6) (29, 30) electrostatic interactions that stabilize the inactive state and suppress basal signaling. In FFAR1, the E/DRY motif is changed to G$^{3.49}$R$^{3.50}$Y$^{3.51}$, and position 6.30 is a positively charged lysine residue such that there is no negatively charged acidic residue to form a salt bridge with R104$^{3.50}$ (Fig. 5*C*). The lack of an intact E/DRY sequence in

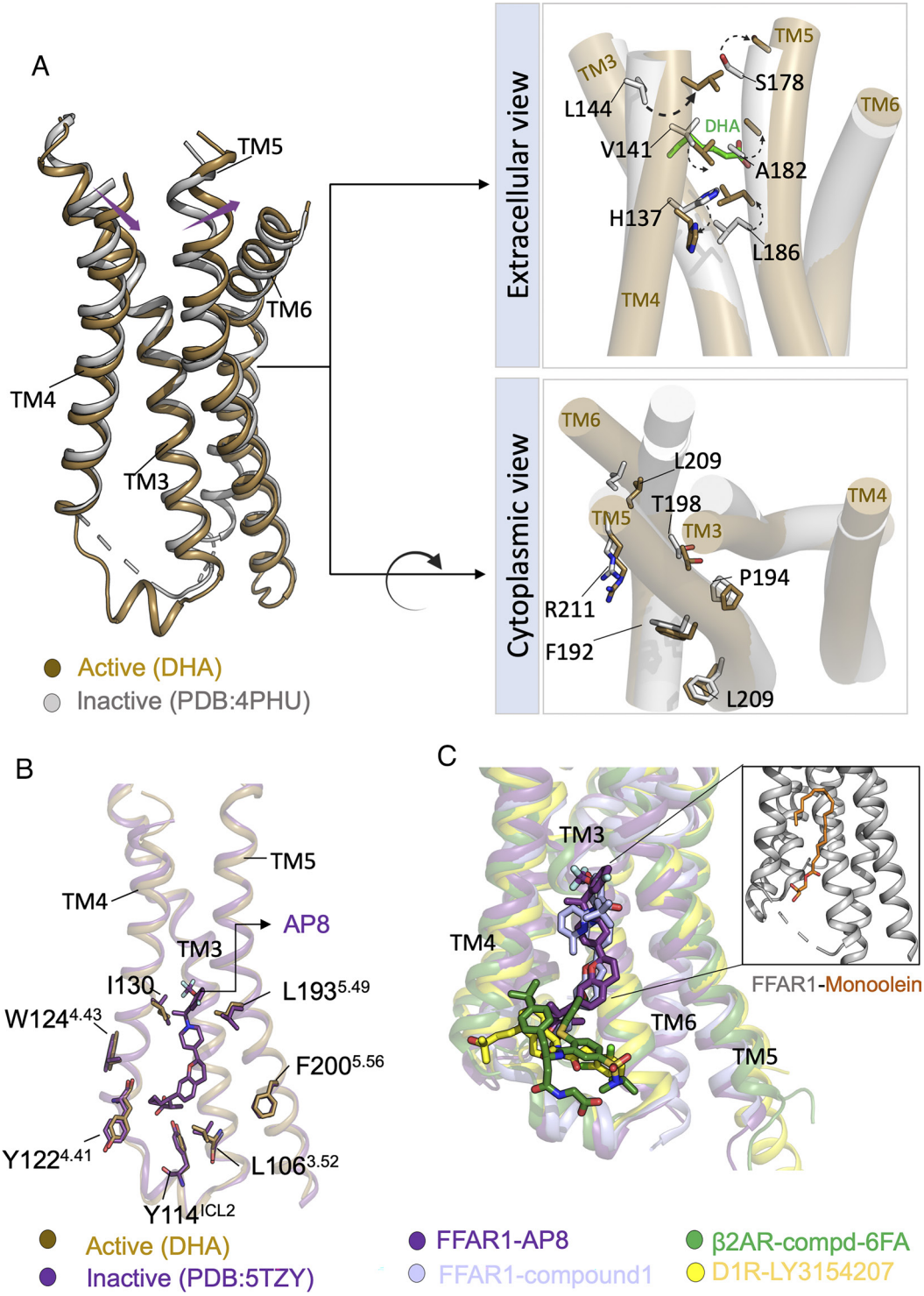

Fig. 6. Allosteric switch in FFAR1 and membrane-embedded AgoPAMs. (*A*, *Left*) Superposition of activated FFAR1 (DHA complex, gold cartoon and sticks) with inactive FFAR1 (PDB: 4PHU, gray sticks), showing the movement of helices (purple arrows). (*A*, *Right Top*) Change in packing of residues on TM4 and TM5 between inactive (gray cylinders and sticks) and activated FFAR1 (gold cylinders and sticks). (*A*, *Right Bottom*) Change in packing of TM domains at the intracellular surface between inactive (gray cylinders and sticks) and activated FFAR1 (gold cylinders and sticks). (*B*) Superposition of activated FFAR1 (DHA complex, gold cartoon and sticks) with AP8-bound inactive FFAR1 (PDB: 5TZY, purple cartoon and sticks). (*C*) Superposition of AP8-bound inactive FFAR1 (PDB: 5TZY, purple cartoon and sticks), compound 1–bound inactive FFAR1 (PDB: 5KW2, light purple cartoon and sticks), Compd-6FA-bound β_2AR (PDB: 6N48, green cartoon and sticks), and LY3154207-bound D1R (PDB: 7X2F, yellow cartoon and sticks). The inset shows the AgoPAM site bound to monoolein in TAK-875-bound FFAR1 (PDB: 4PHU, gray cartoon and orange sticks).

FFAR1 is almost unique among class A GPCRs (including other FFARs). When we mutated G103$^{3.49}$ to aspartate to reconstitute a DRY motif, the resulting construct exhibited diminished G_q signaling activity in response to fatty acids or TAK-875 (*SI Appendix*, Fig. S8*C*). We propose that the lack of an E/DRY motif in FFAR1 sensitizes the receptor to respond to fatty acids by energetically favoring the active-state conformation at the G-protein-coupling site, potentially contributing to the measurement of constitutive activity for the receptor (31, 32). As such, less free energy transmitted from orthosteric agonist binding is needed to promote the active conformation.

Switches involved in allosteric transmission from the orthosteric pocket to the G-protein-binding site are also divergent in FFAR1 relative to most other class A GPCRs. The "toggle switch" residue on TM6 at the base of the orthosteric pocket is an aromatic amino acid in many receptors (33), and this residue changes conformation and moves outward from the core in multiple activated GPCR structures(34). In FFAR1, V237$^{6.48}$ occupies the toggle switch position instead of tryptophan, and this residue remains in a similar position between inactive and active conformations (Fig. 5*D*). Likewise, the "PIF transmission switch" resides at the TM3/5/6 interface halfway between orthosteric and G protein pockets and undergoes packing rearrangements between the inactive and active states of many GPCRs to facilitate the outward movement of TM6 (26, 35). In FFAR1, the amino acid analogous to the "PIF" switch are P194$^{5.50}$/G94$^{3.40}$/L233$^{6.44}$, and these residues do not undergo major repacking between inactive-state crystal structures and our active-state cryo-EM structures (Fig. 5*E*).

Discussion

Consistent with the divergent sequence motifs in FFAR1 and the lack of structural changes in the canonical transmission switches between inactive and active conformations, we propose that activation in this receptor occurs through an alternate mechanism that evolved to accommodate the unusual mode of orthosteric agonist binding. In this framework, fatty acids enter the receptor's orthosteric site through the membrane, accommodated by fluctuations in the position of the extracellular half of TM3 (Fig. 4). The consequences of fatty acid binding are shown by comparison of the inactive-state crystal structures (8, 9, 11) and our active-state cryo-EM structures. When DHA or TAK-875 binds the receptor, with a terminal carboxylic acid in the core and an aliphatic chain wedged between TM3 and TM4 (Fig. 2), the extracellular half of TM4 rotates and shifts closer to TM5 such that L144$^{4.63}$ packs against S178$^{5.34}$, V141$^{4.60}$ pushes against A182$^{5.38}$, and the H137$^{4.56}$ side chain moves away from L186$^{5.42}$ (Fig. 6 *A*, *Top*). When this microswitch is activated, the upper half of TM5 moves toward TM6 with slightly altered packing at every helical turn. Meanwhile, the cytoplasmic half of TM5 undergoes a rigid-body shift along with the upper half, which subtly rotates its side chains to favor packing with the outward-shifted conformation of TM6 (Fig. 6 *A*, *Bottom*). The residues involved in the initiating microswitch in FFAR1 are not highly conserved in the other FFARs, which have the bulkier amino acids valine (FFAR2/3) or tryptophan (FFAR4) in place of A182$^{5.38}$. The major structural changes between inactive and active conformations are not evident in the core of FFAR1 directly under the agonist (Fig. 5 *D* and *E*) but rather consist of these subtle alterations in packing of TMs 4, 5, and 6 propagated along the periphery of the TM helical bundle.

AgoPAM ligands such as AP8 and compound 1 bind in an extrahelical groove formed by ICL2 and the lipid-facing surfaces of TMs 3, 4, and 5 (8, 9). The conformations of TM4 and TM5 and associated helical packing in previous AgoPAM-bound structures are similar to the conformations of these helices in our activated FFAR1 structures without AgoPAMs (Fig. 6*B*), with the notable difference that the cytoplasmic end of TM6 is not shifted outward as in our G protein complexes. AgoPAM binding independently stabilizes a helical conformation for ICL2 (8, 9), which is important for G_q recognition as described above (Fig. 5*A*). Our active-state structures and functional data, combined with previous structures, indicate that FFAR1 AgoPAMs achieve full activation of G_q signaling by bypassing the orthosteric pocket and directly stabilizing an activated conformation of TM4, ICL2, and TM5 in the inner leaflet. Full agonism by these ligands is possible because FFAR1's native fatty acid activation mechanism leads through these same helices.

The interaction of an allosteric modulator at this site is not unique to FFAR1. Indeed, small-molecule positive allosteric modulators have been discovered for β_2AR (36) and D1R (37) that overlap with AP8 and compound 1 (Fig. 6*C*). A distinction of the allosteric site in FFAR1 is that ligands such as AP8 extend deep into the membrane (Fig. 6*C*) so that they can make additional hydrophobic interactions with the receptor. This site could have arisen as a natural interaction surface for lipid tails within the plasma membrane, which is implied by the binding of an ordered monoolein from the lipidic cubic phase in previous crystal structures without AgoPAMs (11). Consurf analysis (38) shows that this site is not highly conserved in other FFARs, providing a potential for subtype-selective agonism (*SI Appendix*, Fig. S9). Exploitation of such lipid-binding surfaces (39) may be a valuable strategy in structure-guided drug design efforts for GPCRs and other membrane proteins, which are currently dominated by targeting of the orthosteric pocket (40). Our structures of FFAR1 highlight the versatility of the GPCR superfamily in converting the energy of agonist binding into G protein activation through diverse allosteric pathways and illustrate how the extrahelical surfaces of GPCRs can be targeted by agonist drugs that bypass the orthosteric pocket and stabilize the active state.

Materials and Methods

Chemicals and Cell Culture. TAK-875 (also known as fasiglifam) was purchased from MedChemExpress (Cat. No. HY-10480). Gamma-linolenic acid (γLA) was purchased from Enzo (Cat. No. 502010798), while DHA was purchased from Acros Organics (Cat. No. 427640010). For functional assays measuring G_q coupling, γLA and DHA were complexed with methyl-b-cyclodextrin (MBCD, Cyclodextrin Technologies Inc).

Cos-7 cells (American Type Culture Collection, Cat. CRL-1651) were cultured and maintained in DMEM (Thermo Fisher) supplemented with 10% Fetal Bovine Serum (FBS) (v/v) (Gibco), penicillin, and streptomycin. HEK293A cells (Thermo Fisher) were cultured and maintained in Dulbecco's Modified Eagle Medium (DMEM) (Nissui Pharmaceutical) supplemented with 5% (v/v) FBS (Corning), glutamine, penicillin, and streptomycin. Cells were cultured in sterile 10-cm plates at 37 °C under 5% CO_2 and passaged at 70 to 80% confluency. Commercial antibodies used in various assays are described in the corresponding sections below.

Cloning and Expression of the Human FFAR1-mGsqiN Complex. The codon-optimized human FFAR1 (hFFAR1) gene bearing an N-terminal HA signal sequence, FLAG tag, and a T4 lysozyme was synthesized (GenScript) and subcloned into the pFastBac vector (Thermo Fisher). The hFFAR1 gene in our cryo-EM structures does not harbor any mutations. Previous inactive-state LCP crystal structures of FFAR1 (8, 9, 11) used four thermostabilizing point mutations that led to slightly decreased agonist and AgoPAM binding (8, 9). None of the previously mutated residues are in contact with the ligands in our cryo-EM structures of the activated wild-type FFAR1 (Fig. 2 *B* and *C*); however, they would be predicted to stabilize the inactive state. F88$^{3.34}$ is at the TM3/TM4 interface near the membrane-facing orthosteric pocket and helps to stabilize the rotated conformation of these helices observed in the G protein complex. L42$^{2.40}$ on

TM1 packs against TM7 close to the G protein interface, stabilizing the ICL1 loop conformation that participates directly in G protein binding. $G103^{3.49}$ is part of the unusual "GRY" sequence seen in FFAR1, which is important in setting the basal activity of the receptor and whose mutation to canonical "DRY" leads to a severe loss of DHA-stimulated signaling (*SI Appendix*, Fig. S8*C*). Residue $Y202^{5.58}$ packs on the outside of TM6, which is shifted outward to accommodate the G protein.

A chimeric mini-G_{α} protein referred to as mG_{sqiN} was cloned into pFastbac, and the human $G_{\beta 1}$ and His_8-tagged $G_{\gamma 2}$ were cloned into the pFastBac dual vector as described previously (13). All baculovirus stocks were made using the ESF 921 media (Expression Systems). For expression of the hFFAR1-mG_{sqiN} complex, all three baculoviruses were coexpressed in a 1:1:1 ratio of hFFAR1:mGsqiN:$G_{\beta 1\gamma 2}$ in *Spodoptera frugiperda* (*Sf9*) cells at a density of 3 to 3.5 × 10^6/mL. Cells were harvested 68 h postinfection, and the pellets were stored at −80 °C.

Cloning, Expression, and Purification of ScFv16. To enable the formation of a stable hFFAR1-mG_{sqiN} complex, the synthetic antibody fragment ScFv16 was used (16, 41). A pFastBac baculovirus encoding ScFv16 and bearing an N-terminal melittin signal sequence and C-terminal His_{10} tag was expressed and secreted from *Sf9* cells and purified as previously described (13). Briefly, ESF 921 media containing the secreted ScFv16 were collected 72 h postinfection by centrifugation of the *Sf9* cells. To balance the pH, 10 mM Tris (pH 8.0) was added. The supernatant was further supplemented with 1 mM Ni_2SO_4 and 5 mM $CaCl_2$ to quench any chelating agents. The supernatant containing ScFv16 was then passed by gravity over Ni-NTA resin. The column was washed with 20 column volumes of buffer containing 50 mM HEPES (pH 7.4), 150 mM NaCl, and 10 mM imidazole to remove nonspecific binding proteins. His-tagged protein was eluted using 50 mM HEPES (pH 7.4), 150 mM NaCl, and 250 mM imidazole. Protein was concentrated and run on a Superdex 200 gel filtration column. The fractions corresponding to monomeric scFv16 were collected and stored at −80 °C.

Purification of hFFAR1-mG_{sqiN}-scFv16 Complexes. To obtain complexes of hFFAR1-mGsqiN-ScFv16 in the presence of either DHA alone or both TAK-875 and γLA, a similar workflow was followed aside from the addition of different ligands. Cell pellets (from 5 L culture) overexpressing hFFAR1, mG_{sqiN}, and $G_{\beta 1\gamma 2}$ were lysed in buffer containing 10 mM HEPES (pH 7.4), 160 μg/mL benzamidine, 100 μg/mL leupeptin, 1 mM $MgCl_2$, 0.1 mM TCEP, apyrase (0.5 mU/mL, NEB), and 50 μM DHA (or 5 μM TAK-875 and 50 μM γLA). The lysate was spun at 10,000 rpm for 20 mins at 4 °C, and the supernatant was discarded. The pellets were resuspended in solubilization buffer containing 50 mM HEPES (pH 7.4), 150 mM NaCl, 10% glycerol, 1 mM $MgCl_2$, 1% (w/v) lauryl maltose neopentyl glycol (LMNG, Anatrace), 0.1% Na cholate, 0.1% cholesteryl hemisuccinate (CHS, Steraloids), 160 μg/mL benzamidine, 100 μg/mL leupeptin, 0.5 mM TCEP, apyrase (15 mU/mL, NEB), 4 mg scFv16, and 200 μM DHA (or 15 μM TAK-875 and 50 μM γLA) and dounced in a dounce homogenizer (Wheaton). The solubilized membranes were incubated for 1 h at 4 °C and ultracentrifuged at 35,000 rpm for 30 min at 4 °C. The supernatant was collected, supplemented with 2 mM $CaCl_2$, and incubated with 5 mL M1 anti-FLAG affinity resin (Sigma-Aldrich, Cat. A4596) in batch mode overnight at 4 °C. Following incubation, the FLAG resin was centrifuged at 1500 rpm and washed with three resin volumes 50 mM HEPES (pH 7.4), 150 mM NaCl, 0.10% GDN, 0.01% CHS, 5% glycerol, 1 mM $MgCl_2$, 2 mM $CaCl_2$, 0.5 mM TCEP, and 100 μM DHA (or 10 μM TAK-875 and 50 μM γLA). The hFFAR1-mG_{sqiN}-scFv16 complex was eluted from the M1 FLAG resin with buffer containing 50 mM HEPES (pH 7.4), 150 mM NaCl, 0.10% GDN, 0.01% CHS, 5% glycerol, 0.5 mM TCEP, 200 μg/mL FLAG, 5 mM EDTA, and 50 μM DHA (or 10 μM TAK-875 and 50 μM γLA). The purified complex was then concentrated and run on a Superose 6 Increase 10/300 size exclusion chromatography column (GE Healthcare) with running buffer containing 20 mM HEPES (pH 7.4), 150 mM NaCl, 0.004% GDN, 0.0004% CHS, 0.5 mM TCEP, and 200 μM for DHA (or 15 μM TAK-875 and 50 μM γLA). Fractions corresponding to the complex peak were collected, analyzed by sodium dodecyl sulfate-polyacrilamide gel electrophoresis (SDS-PAGE), and further concentrated to 8 mg/mL for cryo-EM sample preparation (*SI Appendix*, Fig. S5 *A* and *B*).

Reconstitution of the hFFAR1-mGsqiN-scFv16 Complex into Nanodiscs. The hFFAR1-mG_{sqiN}-scFv16 complex (with TAK-875 and γLA) was reconstituted into nanodiscs using a previously described protocol (42, 43). Briefly, the purified complex was mixed with the membrane scaffolding protein MSP1D1 (15) and a mixture of lipids (POPC: POPG: cholesterol = 2:3:1) at a molar ratio of 1:2.5:200. The mixture was then allowed to incubate for 1 h at 4 °C. Following incubation, the reconstituted mixture was added into a tube containing 75 μL washed Bio-Beads SM2 (50 mg/mL; Bio-Rad) and further incubated for 1 h at 4 °C. After 1-h incubation, the reconstituted mixture was transferred to a tube containing fresh bio-beads, and this procedure was repeated five times. After the final incubation, the mixture was run over a Superose six gel-filtration column in nondetergent running buffer containing 20 mM HEPES (pH 7.4), 150 mM NaCl, 0.5 mM TCEP, 15 μM TAK-875, and 50 μM γLA. Fractions corresponding to the complex peak were collected, analyzed by SDS-PAGE, and further concentrated to 8 mg/mL for cryo-EM grid preparation (*SI Appendix*, Fig. S5*C*).

Cryo-EM Grid Preparation and Data Acquisition. The procedure for freezing grids was the same for all samples. Three microliters of purified protein at 8 mg/mL was applied to a glow-discharged Quantifoil R1.2/1.3 300-mesh Au holey carbon grid (Quantifoil Micro Tools GmbH, Germany) and flash frozen in liquid ethane using a Mark IV Vitrobot (Thermo Fisher Scientific). Cryo-EM micrographs were collected on a Titan Krios microscope operated at 300 kV and equipped with a K3 direct electron detector (Gatan). Movies were recorded in super-resolution correlated double sampling counting mode using a slit width of 20 eV on a GIF-Quantum energy filter. A magnification of 81,000 (corresponding to a pixel size of 1.07 Å) and a defocus range from −1.4 to −2.4 μm were used. Each movie had 50 frames with a total exposure of 9 s. The cumulative electron dose and dose rate varied across the different datasets, details of which are summarized in *SI Appendix*, Table S1.

Cryo-EM Image Processing. The general workflow for image processing was similar for all three datasets generated (*SI Appendix*, Figs. S1–S3). Movie frames of the hFFAR1-mG_{sqiN}-scFv16 complex in the presence of different ligands were processed in Relion 3.1 (44). Briefly, dose-fractioned images were gain normalized, binned two-fold to obtain a pixel size of 1.07 Å, motion corrected, and dose weighted using MotionCor2 (45). The contrast transfer function was corrected using GCTF (46). Roughly 20,000 particles were manually picked and then subjected to 2D classification. Subsequently, the class averages that best represented the projections of the hFFAR1-mG_{sqiN}-scFv16 complex in different orientations were selected as templates for further automated picking. The resulting particles were then extracted, binned 4× (pixel size 4.28 Å), and subjected to 2D classification. Particles showing good features in the 2D classes were selected and subsequently subjected to 3D classification using a de novo initial model generated by RELION as a reference. After 2 to 3 rounds of 3D classification, the classes showing the best secondary structure features were selected for refinement. Density subtraction was performed using a mask to remove micellar density, and 3D refinement of density-subtracted particles showed improved TM helices. The resultant particles were subjected to CTF refinement and particle polishing to generate a final 3D refinement and postprocessed sharpened map with resolutions (using the gold standard FSC criterion) reported in *SI Appendix*, Table S1. Local resolution maps were calculated using Relion 3.1.

Model Building and Refinement. Initial model building was carried out using the hFFAR1-mG_{sqiN}-scFv16/nanodisc structure. The previous structure of FFAR1 (8) (PDB: 5TZY) and the structure of mini-$G_{aq\beta 1\gamma 2}$ with ScFv16 (13) (PDB: 4ZJ8) were used as initial models. The PDB models were first docked into the cryo-EM density map in Coot v. 0.9.4.1 (47). A full model was built in Coot and subjected to multiple rounds of iterative real-space refinement in Phenix v. 1.19.2 (48) followed by manual corrections in Coot. The final model of hFFAR1-mG_{sqiN}-scFv16 in nanodisc (in the presence of TAK-875 and γLA) was used as an initial model and docked into the cryo-EM density maps of other reconstructions, which were then subjected to iterative refinement as described above. Initial coordinates and refinement parameters for the ligands DHA (truncated at C7), TAK-875, and γLA were prepared using the DRG web server (http://davapc1.bioch.dundee.ac.uk/cgi-bin/prodrg). MolProbity was used to assess the final model geometries as a part of Phenix validation tools. Statistics for data collection and refinement are shown in *SI Appendix*, Table S1. Cryo-EM density maps were deposited in the Electron Microscopy Data Bank under accession codes EMD-28164 (DHA complex), EMD28177 (TAK-875 and γLA), EMD28185 (TAK-875 and γLA, nanodisc). Atomic coordinates were deposited in the PDB under accession codes 8EIT (DHA complex), 8EJC (TAK-875 and γLA), and 8EJK (TAK-875 and γLA, nanodisc). Structure figures were made using Pymol v. 2.5 (Schrödinger, LLC) and UCSF Chimera v. 1.3 (49). In the hFFAR1-mG_{sqiN} structure with DHA, residues 149 to 155 and 165 to 166 of ECL2 were omitted due to weak density. In the hFFAR1-mG_{sqiN} structures in the presence of TAK-875 and γLA, residues 149 to 155 were omitted.

Preparation of Fatty Acid/MBCD Complexes. To prevent lipotoxicity, γLA and DHA were delivered to cells as MBCD complexes (50). To prepare these complexes, 20 mL of 15 mM MBCD was heated to 70 °C and slowly titrated with 30 mM DHA or γLA over 1 h until the solution turned clear. The resulting solutions were then allowed to cool to room temperature and stirred overnight and then lyophilized at −80 °C. Solutions were resuspended in water to produce a final concentration of 30 mM MBCD:4 mM DHA or 30 mM MBCD:6 mM γLA. To ensure that fatty acids DHA and γLA had not been oxidized or otherwise modified during the preparation of MBCD complexes, 15 mg samples of each fatty acid/MBCD complex were subjected to organic extraction using 3 mL ethyl acetate: 3 mL water with ~100 μL 10% HCL. The pure fatty acid was isolated in the ethyl acetate layer and then subjected to ^{1}H and proton-decoupled ^{13}C NMR analysis (chloroform-D as a solvent for γLA; acetone-D6 as a solvent for DHA) on a Bruker 600-MHz NMR spectrometer. Chemical shifts are reported in parts per million (ppm) from low to high field relative to a residual solvent. NMR spectra of the fatty acids extracted from the MBCD complexes were compared to control samples of fatty acids that had undergone no complex formation (*SI Appendix*, Fig. S10), showing that there is no observable oxidation or other modification of these compounds caused by MBCD complex formation.

IP Accumulation Assay for G_q Signaling. For measuring G_q-based signaling, an IP accumulation assay was used as previously described (13, 51). Cos-7 cells were used for the assay and maintained in DMEM-high glucose (Millipore Sigma) supplemented with 10% FBS (Corning) and 1% penicillin–streptomycin (Millipore Sigma). All receptor constructs used for the assay bear an N-terminal HA signal sequence, FLAG tag, and T4-lysozyme, as with cryo-EM constructs. For functional assays, the receptor constructs were cloned into pcDNA3.1. The EC_{50} values for wild-type hFFAR1 with or without the N-terminal T4L were shown to be identical (*SI Appendix*, Fig. S8*D*); however, the expression level of the T4L-bearing constructs was higher, leading to their use as wild-type background. To further enhance the E_{max} for the IP accumulation assay, a plasmid encoding full-length human G_{aq}(52) was cotransfected with hFFAR1 constructs into Cos-7 cells (1.1×10^6 cells per 10 cm dish) using Lipofectamine 3,000 (Thermo Fisher). After 24 h, the cells were plated on poly-D-lysine (0.01%) coated 96-well clear-bottom tissue culture plates (Perkin Elmer) at 20,000 cells/well in inositol-free DMEM (MP Biomedicals) supplemented with 10% FBS, 4 mM L-glutamine (Millipore Sigma), penicillin-streptomycin, and 5 μCi/ml myo-[2-^{3}H] inositol (Perkin Elmer). Twenty-four hours after plating, the media were replaced with HBSS media (Millipore Sigma) containing 10 mM LiCl and supplemented with agonists (varying concentrations of DHA/MBCD, TAK-875, or γLA/MBCD). The plates were incubated at 37 °C for 75 min. Subsequently, the agonist solutions were removed, and cells were lysed on ice for 30 min with 10 mM formic acid (Millipore Sigma). Then, 1.25 mg of polylysine-coated YSI SPA beads (Perkin Elmer) was added to each well. The plates were mixed on an orbital shaker for 30 min and then analyzed on a MicroBeta scintillation counter (Perkin Elmer) after 8 h. For the PAM assay (Fig. 3 *C* and *D* and *SI Appendix*, Table S2*B*), the same protocol was followed as described above, except varying concentrations of TAK-875 at 2× (with 10 μM being the highest) were prepared in the LiCl-HBSS buffer. Fifty microliters from each of the different dilutions was added to each well. This was followed by the addition of 50 μL of 2× concentration of γLA/MBCD or DHA/MBCD diluted in the same LiCl-HBSS buffer. IP accumulation assays on different constructs were performed in at least three independent experiments, each carried out in duplicate. MicroBeta cpm data were normalized to hFFAR1 wild-type E_{max}, and dose responses were fitted to the four-parameter model "log(agonist) vs. response" for TAK-875 and four parameters for free-fatty acid agonists in GraphPad Prism 9 (GraphPad Software). Fitted pEC_{50} values were analyzed for statistical significance compared to hFFAR1 wild type using one-way ANOVA followed by Dunnett's test. All pharmacological parameters are displayed in *SI Appendix*, Table S2 *A*–*C*.

TGFα Shedding Assay for G_q Signaling. TGFα shedding assay was performed as described previously (20), with minor modifications. HEK293A cells (Thermo Fisher) were seeded in a 6-cm culture dish (Greiner Bio-One) at a concentration of 2×10^5 cells/ml (4 mL per dish hereafter) in DMEM (Nissui Pharmaceutical) supplemented with 5% (v/v) FBS (Gibco), glutamine, penicillin, and streptomycin 1 d before transfection. The transfection solution was prepared by combining 10 μL of 1 mg/mL polyethylenimine Max solution (Polysciences) and a plasmid mixture consisting of 80 ng T4L-FFAR1, 1 μg alkaline phosphatase (AP)-tagged TGFα (AP-TGFα; human codon-optimized), and 920 ng empty pCAGGS plasmid. One day after incubation, the transfected cells were harvested by trypsinization, neutralized with DMEM containing 5% (v/v) FBS and penicillin–streptomycin, washed once with Hank's Balanced Salt Solution (HBSS) containing 5 mM HEPES (pH 7.4), and resuspended in 13.5 mL (agonist assay) or 12 mL (PAM assay) of HEPES-containing HBSS. For the agonist assay (*SI Appendix*, Fig. S7 *A* and *B*), the cell suspension was seeded into a 96-well plate (Greiner Bio-One) at a volume of 90 μL (per well hereafter) and incubated for 30 min in a CO_2 incubator. Test FFAR1 agonists γLA/MBCD, DHA/MBCD, or TAK-875 diluted in 0.01% (w/v) BSA- and 5 mM HEPES-containing HBSS (at 10x concentration) or vehicle were added at a volume of 10 μL, and the plate was incubated for 1 h. For the PAM assay (Fig. 3*D*), the transfected cells were resuspended in 12 mL of the HEPES-containing HBSS and seeded into the 96-well plate at a volume of 80 μL and incubated for 30 min in the CO2 incubator. Test FFAR1 PAM γLA/MBCD or DHA/MBCD diluted in 0.01% (w/v) BSA, 5 mM HEPES-containing HBSS (at 10× concentration), or vehicle was added at a volume of 10 μL. After 5 min, a test FFAR1 agonist (TAK-875; serially diluted in 0.01% (w/v) BSA and 5 mM HEPES-containing HBSS at 10x concentration) was added, and the plate was incubated for 1 h. After centrifugation, conditioned media (80 μL) were transferred to an empty 96-well plate. AP reaction solution (10 mM p-nitrophenylphosphate (p-NPP), 120 mM Tris–HCl (pH 9.5), 40 mM NaCl, and 10 mM MgCl2) was dispensed into the cell culture plates and plates containing conditioned media (80 μL). Absorbance at 405 nm was measured before and after 2 h incubation at room temperature using a microplate reader (SpectraMax 340 PC384; Molecular Devices). Ligand-induced AP-TGFα release was calculated as described previously (20), with an additional normalization to set a receptor-independent positive control signal by 1 μM 12-O-tetradecanoylphorbol 13-acetate as 100%. Unless otherwise noted, vehicle-treated (i.e., without PAM and agonist treatment) AP-TGFα release signal was set as a baseline. Using Prism 9 software (GraphPad Prism), AP-TGFα release signals were fitted with a four-parameter sigmoidal concentration–response curve with a constraint of the HillSlope to absolute values less than 1.5. For each replicate experiment, the parameters Span (= Top – Bottom) and pEC_{50} of individual FFAR1 mutants were normalized to those of wild-type FFAR1 performed in parallel, and the resulting E_{max} and pEC_{50} values were used to calculate the ligand response of the mutants.

MD Simulation. MD simulations were performed on a system using the activated FFAR1 receptor polypeptide derived from the DHA-bound FFAR1-mG_{sqiN}-scFv16 complex, either with or without DHA from the model. The receptor was oriented with respect to the membrane normal with the PPM web server (53) and then inserted into a heterogeneous lipid bilayer model that contains unsaturated acyl lipid (POPC), saturated acyl lipid (DPPC), and cholesterol in a ratio of 2:2:1. Overlapped lipids were removed after the insertion. Then, the system was solvated into a TIP3P water box (54) with size 81 × 81 × 97 Å. Na^+ and Cl^- ions were randomly placed to neutralize the system. After the initial system was set up, a short steepest descent energy minimization was performed to remove the energetically unfavorable contacts. Then, the whole system was heated from 0 to 303.15 K using velocity rescaling and equilibrated for 1.0 ns in the NPT ensemble with the harmonic restraints on the backbone atoms of the protein and the head group atoms of the lipids removing gradually. A 210-ns production run without any restraints was applied to the system after the equilibration. All the MD simulations involved in this study were performed by the GPU version of NAMD 2.14 package (55) with periodic boundary conditions. CHARMM36 force field (56) was applied to all the models. The Nosé–Hoover Langevin piston pressure control and Langevin damping dynamics (57) were employed to keep the simulated systems at a constant pressure of one atmosphere and a constant temperature of 303.15 K. The long-range electrostatic interactions were evaluated by the particle mesh Ewald (PME) method (58) with the size of the grid at about 1 Å. The full PME was calculated at every step. The van der Waals interactions were treated by using a cutoff of 12 Å. All the simulations were performed with a time step of 1 fs.

Whole-Cell ELISA for Measuring Surface Expression. To measure surface expression, a whole-cell ELISA method was used as previously described (13). Briefly, Cos-7 or HEK293 cells were cotransfected with receptor constructs and G_q (as described for the IP accumulation and TGFa assays) and overexpression and incubated for 24 h. Cells were washed 2× with TBS, fixed with 4% paraformaldehyde for 20 min on ice, and then blocked for 1 h at room temperature

with 1% w/v BSA in TBS. Subsequently, the cells were incubated for 1 h at room temperature with 9.7 μg/mL of M1-Flag antibody (Sigma Aldrich, Cat. F3040), washed 3× with blocking buffer, and then incubated with HRP-coupled secondary antibody (Jackson ImmunoResearch, Cat. 715-035-150) (1:2,000 dilution in blocking buffer) for 1 h at room temperature. To visualize surface expression, 200 μL tetramethylbenzidine ELISA (Thermo Fisher) was added, and absorbance at 450 nm was read using a CLARIOstar microplate reader (BMG LABTECH). After measuring HRP activity, cells were washed with TBS and then incubated with 200 μL/well of 0.2% (w/v) Janus green for 20 min. Cells were then washed 3×, and 800 μL/well of 0.5 M HCl was added. Absorbance at 595 nm was recorded on the CLARIOstar. For each well condition, the normalized cell surface expression was determined by dividing absorbance at 450 nm by absorbance at 595 nm. Experiments were repeated three times. The data were analyzed by one-way ANOVA (and nonparametric or mixed) and plotted as a column with scattered points using GraphPad Prism 9 (GraphPad Software).

Data, Materials, and Software Availability. Structural models have been deposited in the Protein Data Bank (PDB) with coordinate accession numbers 8EIT (59), 8EJC (60), and 8EJK (61). Cryo-EM maps have been deposited in the Electron Microscopy Data Bank (EMDB) with accession numbers EMD-28164 (62), EMD-28177 (63), and EMD-28185 (64).

ACKNOWLEDGMENTS. This work was supported by the NIH (R35GM116387 to D.M.R.) and the Welch Foundation (I-1770 to D.M.R.). A.I. was funded by Japan Society for the Promotion of Science KAKENHI grants 21H04791, 21H05113, JPJSBP120213501, and JPJSBP120218801; JPMJFR215Tand JPMJMS2023 from the Japan Science and Technology Agency; JP22ama121038 and JP22zf0127007 from the Japan Agency for Medical Research and Development. Molecular Dynamics simulation studies were supported by the BioHPC supercomputing facility in the Lyda Hill Department of Bioinformatics, UT Southwestern Medical Center. Cryo-EM data were collected at the University of Texas Southwestern Medical Center Cryo-EM Facility, which is funded by the Cancer Prevention and Research Institute of Texas Core Facility Support Award RP170644. We thank Minwoo Kim from the University of Texas Southwestern Biochemistry Department for help with collecting NMR data; Kayo Sato, Shigeko Nakano and Ayumi Inoue at Tohoku University for their assistance in plasmid preparation and the cell based GPCR assays.

1. I. Kimura, A. Ichimura, R. Ohue-Kitano, M. Igarashi, Free fatty acid receptors in health and disease. *Physiol. Rev.* **100**, 171–210 (2020).
2. G. Milligan, B. Shimpukade, T. Ulven, B. D. Hudson, Complex pharmacology of free fatty acid receptors. *Chem. Rev.* **117**, 67–110 (2017).
3. Y. Itoh *et al.*, Free fatty acids regulate insulin secretion from pancreatic β cells through GPR40. *Nature* **422**, 173–176 (2003).
4. C. P. Briscoe *et al.*, The orphan G protein-coupled receptor GPR40 is activated by medium and long chain fatty acids*. *J. Biol. Chem.* **278**, 11303–11311 (2003).
5. Z. Li, Z. Zhou, L. Zhang, Current status of GPR40/FFAR1 modulators in medicinal chemistry (2016–2019): A patent review. *Expert Opin. Ther. Pat.* **30**, 1–12 (2019).
6. J. S. Shavadia *et al.*, Determination of fasiglifam-induced liver toxicity: Insights from the data monitoring committee of the fasiglifam clinical trials program. *Clin. Trials* **16**, 253–262 (2019).
7. P. Governa *et al.*, FFAR1/GPR40: One target, different binding sites, many agonists, no drugs, but a continuous and unprofitable tug-of-war between ligand lipophilicity, activity, and toxicity. *Bioorg. Med. Chem. Lett.* **41**, 127969 (2021).
8. J. Lu *et al.*, Structural basis for the cooperative allosteric activation of the free fatty acid receptor GPR40. *Nat. Struct. Mol. Biol.* **24**, 570–577 (2017).
9. J. D. Ho *et al.*, Structural basis for GPR40 allosteric agonism and incretin stimulation. *Nat. Commun.* **9**, 1645 (2018).
10. M. Grundmann, E. Bender, J. Schamberger, F. Eitner, Pharmacology of free fatty acid receptors and their allosteric modulators. *Int. J. Mol. Sci.* **22**, 1763 (2021).
11. A. Srivastava *et al.*, High-resolution structure of the human GPR40 receptor bound to allosteric agonist TAK-875. *Nature* **513**, 124–127 (2014).
12. J. A. Ballesteros, H. Weinstein, Integrated methods for the construction of three-dimensional models and computational probing of structure-function relations in G protein-coupled receptors. *Methods Neurosci.* **25**, 366–428 (1995).
13. J. Yin *et al.*, Molecular mechanism of the wake-promoting agent TAK-925. *Nat. Commun.* **13**, 2902 (2022).
14. C. Yabuki *et al.*, A novel antidiabetic drug, fasiglifam/TAK-875, acts as an Ago-allosteric modulator of FFAR1. *Plos One* **8**, e76280 (2013).
15. I. G. Denisov, Y. V. Grinkova, A. A. Lazarides, S. G. Sligar, Directed self-assembly of monodisperse phospholipid bilayer nanodiscs with controlled size. *J. Am. Chem. Soc.* **126**, 3477–3487 (2004).
16. S. Maeda *et al.*, Development of an antibody fragment that stabilizes GPCR/G-protein complexes. *Nat. Commun.* **9**, 3712 (2018).
17. C. S. Sum, I. G. Tikhonova, S. Costanzi, M. C. Gershengorn, Two arginine-glutamate ionic locks near the extracellular surface of FFAR1 gate receptor activation*. *J. Biol. Chem.* **284**, 3529–3536 (2009).
18. I. G. Tikhonova *et al.*, Bidirectional, iterative approach to the structural delineation of the functional "Chemoprint" in GPR40 for agonist recognition. *J. Med. Chem.* **50**, 2981–2989 (2007).
19. D.C.-H. Lin *et al.*, Identification and pharmacological characterization of multiple allosteric binding sites on the free fatty acid 1 receptor. *Mol. Pharmacol.* **82**, 843–859 (2012).
20. A. Inoue *et al.*, TGFα shedding assay: An accurate and versatile method for detecting GPCR activation. *Nat. Methods* **9**, 1021–1029 (2012).
21. G. K. Balendiran *et al.*, Crystal structure and thermodynamic analysis of human brain fatty acid binding protein. *J. Biol. Chem.* **275**, 27045–27054 (2000).
22. S. Maeda, Q. Qu, M. J. Robertson, G. Skiniotis, B. K. Kobilka, Structures of the M1 and M2 muscarinic acetylcholine receptor/G-protein complexes. *Science* **364**, 552–557 (2019).
23. K. Kim *et al.*, Structure of a hallucinogen-activated Gq-Coupled 5-HT2A serotonin receptor. *Cell* **182**, 1574–1588.e19 (2020).
24. J. I. Mobbs *et al.*, Structures of the human cholecystokinin 1 (CCK1) receptor bound to Gs and Gq mimetic proteins provide insight into mechanisms of G protein selectivity. *Plos Biol.* **19**, e3001295 (2021).
25. Q. Liu *et al.*, Ligand recognition and G-protein coupling selectivity of cholecystokinin A receptor. *Nat. Chem. Biol.* **17**, 1238–1244 (2021).
26. S. G. F. Rasmussen *et al.*, Crystal structure of the β2 adrenergic receptor-Gs protein complex. *Nature* **477**, 549–555 (2011).
27. S. G. F. Rasmussen *et al.*, Crystal structure of the human beta2 adrenergic G-protein-coupled receptor. *Nature* **450**, 383–387 (2007).
28. D. M. Rosenbaum *et al.*, GPCR engineering yields high-resolution structural insights into beta2-adrenergic receptor function. *Science* **318**, 1266–1273 (2007).
29. J. A. Ballesteros, Activation of the beta 2-adrenergic receptor involves disruption of an ionic lock between the cytoplasmic ends of transmembrane segments 3 and 6. *J. Biol. Chem.* **276**, 29171–29177 (2001).
30. S. Vanni, M. Neri, I. Tavernelli, U. Rothlisberger, Observation of "ionic lock" formation in molecular dynamics simulations of wild-type beta 1 and beta 2 adrenergic receptors. *Biochemistry* **48**, 4789–4797 (2009).
31. L. A. Stoddart, A. J. Brown, G. Milligan, Uncovering the pharmacology of the G protein-coupled receptor GPR40: High apparent constitutive activity in guanosine 5′-O-(3-[35S]thio)triphosphate binding studies reflects binding of an endogenous agonist. *Mol. Pharmacol.* **71**, 994–1005 (2007).
32. L. A. Stoddart, G. Milligan, Chapter twenty-eight constitutive activity of GPR40/FFA1 intrinsic or assay dependent? *Methods Enzymol.* **484**, 569–590 (2010).
33. L. Shi *et al.*, Beta2 adrenergic receptor activation. Modulation of the proline kink in transmembrane 6 by a rotamer toggle switch. *J. Biol. Chem.* **277**, 40989–40996 (2002).
34. K. K. Kumar *et al.*, Structure of a signaling cannabinoid receptor 1-G protein complex. *Cell* **176**, 448–458.e12 (2019).
35. W. Huang *et al.*, Structural insights into μ-opioid receptor activation. *Nature* **524**, 315–321 (2015).
36. X. Liu *et al.*, Mechanism of β2AR regulation by an intracellular positive allosteric modulator. *Science* **364**, 1283–1287 (2019).
37. X. Teng *et al.*, Ligand recognition and biased agonism of the D1 dopamine receptor. *Nat. Commun.* **13**, 3186 (2022).
38. H. Ashkenazy *et al.*, ConSurf 2016: An improved methodology to estimate and visualize evolutionary conservation in macromolecules. *Nucleic Acids Res.* **44**, W344–W350 (2016).
39. J. Payandeh, M. Volgraf, Ligand binding at the protein–lipid interface: Strategic considerations for drug design. *Nat. Rev. Drug Discov.* **20**, 710–722 (2021).
40. E. A. Fink *et al.*, Structure-based discovery of nonopioid analgesics acting through the α2A-adrenergic receptor. *Science* **377**, eabn7065 (2022).
41. A. Koehl *et al.*, Structure of the μ-opioid receptor-Gi protein complex. *Nature* **558**, 547–552 (2018).
42. M. R. Whorton *et al.*, A monomeric G protein-coupled receptor isolated in a high-density lipoprotein particle efficiently activates its G protein. *Proc. Natl. Acad. Sci. U.S.A.* **104**, 7682–7687 (2007).
43. J. Yin *et al.*, Structure of a D2 dopamine receptor-G-protein complex in a lipid membrane. *Nature* **584**, 125–129 (2020).
44. J. Zivanov *et al.*, New tools for automated high-resolution cryo-EM structure determination in RELION-3. *Elife* **7**, 163 (2018).
45. S. Q. Zheng *et al.*, MotionCor2: Anisotropic correction of beam-induced motion for improved cryo-electron microscopy. *Nat. Meth* **14**, 331–332 (2017).
46. K. Zhang, Gctf: Real-time CTF determination and correction. *J. Struct. Biol.* **193**, 1–12 (2016).
47. P. Emsley, B. Lohkamp, W. G. Scott, K. Cowtan, Features and development of Coot. *Acta Crystallogr. D Biol. Crystallogr.* **66**, 486–501 (2010).
48. D. Liebschner *et al.*, Macromolecular structure determination using X-rays, neutrons and electrons: Recent developments in Phenix. *Acta Crystallogr. D Struct. Biol.* **75**, 861–877 (2019).
49. E. F. Pettersen *et al.*, UCSF Chimera–A visualization system for exploratory research and analysis. *J. Comput. Chem.* **25**, 1605–1612 (2004).
50. K. Brunaldi, N. Huang, J. A. Hamilton, Fatty acids are rapidly delivered to and extracted from membranes by methyl-beta-cyclodextrin. *J. Lipid Res.* **51**, 120–131 (2009).
51. J. M. Mathiesen, M. T. Ramirez, The metabotropic glutamate receptor 4 is internalized and desensitized upon protein kinase C activation. *British J. Pharmacol.* **148**, 279–290 (2006).
52. J. R. Hepler *et al.*, Functional importance of the amino terminus of Gqα (∗). *J. Biol. Chem.* **271**, 496–504 (1996).
53. A. L. Lomize, S. C. Todd, I. D. Pogozheva, Spatial arrangement of proteins in planar and curved membranes by PPM 3.0. *Protein Sci.* **31**, 209–220 (2022).
54. W. L. Jorgensen, J. Chandrasekhar, J. D. Madura, R. W. Impey, M. L. Klein, Comparison of simple potential functions for simulating liquid water. *J. Chem. Phys.* **79**, 926–935 (1983).
55. J. C. Phillips *et al.*, Scalable molecular dynamics on CPU and GPU architectures with NAMD. *J. Chem. Phys.* **153**, 044130 (2020).
56. J. Huang *et al.*, CHARMM36m: An improved force field for folded and intrinsically disordered proteins. *Nat. Methods* **14**, 71–73 (2017).
57. W. G. Hoover, Canonical dynamics: Equilibrium phase-space distributions. *Phys. Rev. A* **31**, 1695–1697 (1985).

58. T. Darden, D. York, L. Pedersen, Particle mesh Ewald: An N ·log(N) method for ewald sums in large systems. *J. Chem. Phys.* **98**, 10089–10092 (1993).
59. P. Kumari *et al.*, Structure of FFAR1-Gq complex bound to DHA. *Protein Data Bank* for 8EIT, http://www.rcsb.org/structure/8EIT. Deposited 15 September 2022.
60. P. Kumari *et al.*, Structure of FFAR1-Gq complex bound to TAK-875. *Protein Data Bank* for 8EJC, http://www.rcsb.org/structure/8EJC. Deposited 16 September 2022.
61. P. Kumari *et al.*, Structure of FFAR1-Gq complex bound to TAK-875 in a lipid nanodisc. *Protein Data Bank* for 8EJK. http://www.rcsb.org/structure/8EJK. Deposited 17 September 2022.
62. P. Kumari *et al.*, Structure of FFAR1-Gq complex bound to DHA. *Electron Microscopy Data Bank* for EMD-28164. http://www.ebi.ac.uk/emdb/EMD-28164. Deposited 15 September 2022.
63. P. Kumari *et al.*, Structure of FFAR1-Gq complex bound to TAK-875. *Electron Microscopy Data Bank* for EMD-28177. http://www.ebi.ac.uk/emdb/EMD-28177. Deposited 16 September 2022.
64. P. Kumari *et al.*, Structure of FFAR1-Gq complex bound to TAK-875 in a lipid nanodisc. *Electron Microscopy Data Bank* for EMD-28185. http://www.ebi.ac.uk/emdb/EMD-28185. Deposited 17 September 2022.